

Chaotic Chimera Attractors in a Triangular Network of Identical Oscillators

Seungjae Lee* and Katharina Krischer†

*Physik-Department, Technische Universität München,
James-Franck-Straße 1, 85748 Garching, Germany*

(Dated: January 18, 2023)

A prominent type of collective dynamics observed in networks of coupled oscillators is the coexistence of coherent and incoherent parts. Such chimera states may possess various ensemble dynamics accompanying different motions of degree of coherence in the asynchronous part. Stationary and periodic chimeras are known to occur in simple two-population networks of identical phase oscillators. The question for the minimal topology that allows for chaotic chimeras is still open. Here, we show that chaotic chimera attractors exist in three populations of identical phase oscillators. They live in finite-sized systems as well as in the thermodynamic limit outside the Ott-Antonsen manifold. Yet, on the Ott-Antonsen manifold, they are rendered periodic, with the global dynamics of the two incoherent populations exhibiting antiphase oscillation.

Understanding the dynamics of ensembles of coupled oscillators is pivotal for applications in many disciplines, examples ranging from laser physics [1, 2] or Josephson junctions [3–5] to biology [6–8] and neural science [9–11]. A most intriguing collective behavior is the coexistence of synchrony and asynchrony in an ensemble of identical oscillators. The peculiarity of such a state was pointed out 20 years ago by Battogtokh and Kuramoto [12], and was later emphasized by dubbing it a chimera state [13].

While originally chimera states were investigated in a spatially extended ring geometry [14–16], simpler settings, in particular two-population networks revealed essential properties of chimera states [17, 18]. Here, a chimera state consists of one fully synchronized and one incoherent populations. The success of this model relied on two pillars: First, the degree of synchrony of each population can be measured with the complex Kuramoto order parameter. Second, dimension reduction methods allow for the investigation of the dynamics of each population in terms of a few global variables. In the thermodynamic limit, an invariant manifold, called Ott-Antonsen (OA) manifold [19–21], exists on which the evolution equation for the complex order parameter can be written in a closed form, so that the evolution of each population is governed by just two variables [18]. For finite-sized systems, a so-called Watanabe-Strogatz (WS) transformation [22] maps the microscopic dynamics of each population to three global variables and $N - 3$ independent constants of motion [23–25].

In two population networks, three types of stable chimera states were identified: Stationary chimera states where the incoherent population possesses a constant degree of partial coherence, and breathing chimeras where the degree of partial coherence oscillates periodically [18, 25, 26], and quasiperiodic chimeras exhibiting quasiperiodic motion of the order parameter [23, 24].

In contrast, chaotic motion of the macroscopic dynamics seems to require more complex settings, such as ensembles of heterogeneous oscillators [27–31] or higher order interactions [32–34] but has not been found in two-population networks of identical phase oscillators. Analyzing the dynamics a bit closer, it is not astonishing that for two-population networks, macroscopic chaos does not occur in the OA manifold. Here, the effective number of degrees of freedom is just two, due to the phase shift invariance of the equation and the fact that the synchronized population does not change its degree of coherence [18]. This is in accordance with the observation that quasiperiodic chimera states were only observed for finite-sized systems in the WS description with non-uniform constants of motion [23, 24]. Yet, also here no chaotic chimera states were detected.

The question, under which conditions macroscopic chaotic chimera states arise in ensembles of identical phase oscillators is still an open problem. In fact, to the best of our knowledge, chaotic chimeras were only observed as chaotic transients in a finite-size ring geometry [27, 28]. In the long-time limit the dynamics collapses to the fully synchronized solution while in the continuum limit the state becomes neutrally stable [35]. In this work, we demonstrate that chaotic chimera attractors exist in what seems to be the next simplest topology after the two-population network: a three-population network of identical phase oscillators globally coupled within each population and arranged in a triangle with equal inter-population coupling strengths.

Consider a system of identical Kuramoto-Sakaguchi phase oscillators, each oscillator j being described by a phase variable $\phi_j^{(a)}(t) \in [-\pi, \pi]$ where $a = 1, 2, 3$ denotes the population of a three-population network and each population consists of N oscillators. The $3N$ microscopic governing equations are given by

$$\frac{d}{dt}\phi_j^{(a)} = \omega + \text{Im}\left[H_a(t)e^{-i\phi_j^{(a)}}\right] \quad (1)$$

with $j = 1, \dots, N$ and $a = 1, 2, 3$. $H_a(t)$ represents a mean-field forcing defined by $H_a(t) := e^{-i\alpha}(\mu\Gamma_a(t) +$

* seungjae.lee@tum.de

† krischer@tum.de

$\nu\Gamma_b(t) + \nu\Gamma_c(t)$ where (a, b, c) is a permutation of $(1, 2, 3)$. $\Gamma_a(t)$ denotes the complex Kuramoto order parameter of each population, which is defined as

$$\Gamma_a(t) = r_a(t)e^{i\Theta_a(t)} := \frac{1}{N} \sum_{j=1}^N e^{i\phi_j^{(a)}(t)}. \quad (2)$$

The phase-lag parameter α is conveniently written as $\alpha = \frac{\pi}{2} - \beta$. In this work, we fix $\beta = 0.025$. Since the oscillators are identical, we can set $\omega = 0$ and the intra-population coupling strength $\mu = 1$. The inter-population coupling strength ν , which we assume to be always weaker than the intra-population coupling strength, is expressed through $\nu = 1 - A$ where $A \in [0, 1]$. Note that the larger the parameter A , the weaker the coupling between populations [36]. In matrix form, the coupling strength of this triangular, symmetric network [37] is thus given by

$$(K_{aa'}) = \begin{pmatrix} \mu & \nu & \nu \\ \nu & \mu & \nu \\ \nu & \nu & \mu \end{pmatrix}$$

for $a, a' = 1, 2, 3$.

Below we analyze the dynamics of Eq. (1) on the levels of the OA and WS reductions. First, we derive the global dynamics of the finite-size system. Therefore, we exploit the WS transformation [21, 22, 24]:

$$e^{i\phi_j^{(a)}} = e^{i\Phi_a} \frac{\rho_a + e^{i(\psi_j^{(a)} - \Psi_a)}}{1 + \rho_a e^{i(\psi_j^{(a)} - \Psi_a)}} \quad (3)$$

for $j = 1, \dots, N$ and $a = 1, 2, 3$. For each population, the radial variable $\rho_a(t)e^{i\Phi_a(t)}$ measures the degree of coherence with the mean phase; note, though, that they are not exactly identical to Γ_a of the Kuramoto order parameter. The second angular variable, $\Psi_a(t)$, specifies the motion of the oscillators with respect to the mean phase and $\{\psi_j^{(a)}\}_{j=1}^N$ are $N - 3$ independent constants of motion that satisfy three constraints: $\sum_{j=1}^N \cos \psi_j^{(a)} = \sum_{j=1}^N \sin \psi_j^{(a)} = 0$ and $\sum_{j=1}^N \psi_j^{(a)} = 0$ for $a = 1, 2, 3$ [21–24]. The WS macroscopic variables are related to the complex Kuramoto order parameter via [23, 24]:

$$\Gamma_a(t) = \rho_a(t)e^{i\Phi_a(t)}\gamma_a(\rho_a, \Psi_a; t) \quad (4)$$

where γ_a is defined by

$$\begin{aligned} \gamma_a &= \frac{1}{\rho_a} (\zeta_a(t) + i\xi_a(t)) \\ &:= \frac{1}{\rho_a N} \sum_{k=1}^N \frac{2\rho_a + (1 + \rho_a^2) \cos(\psi_k^{(a)} - \Psi_a)}{1 + 2\rho_a \cos(\psi_k^{(a)} - \Psi_a) + \rho_a^2} \\ &\quad + i \frac{1}{\rho_a N} \sum_{k=1}^N \frac{(1 - \rho_a^2) \sin(\psi_k^{(a)} - \Psi_a)}{1 + 2\rho_a \cos(\psi_k^{(a)} - \Psi_a) + \rho_a^2} \end{aligned} \quad (5)$$

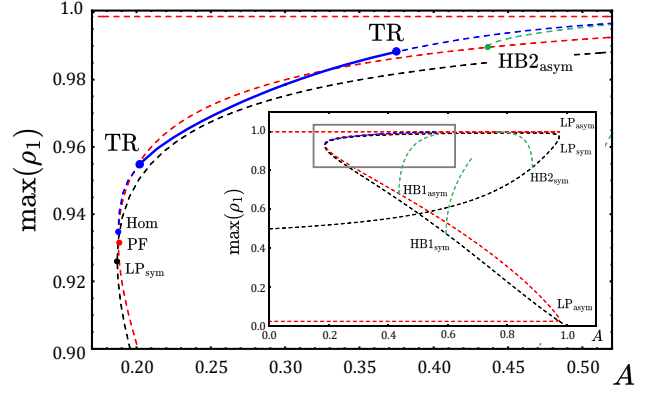


FIG. 1. Bifurcation diagram of DSD-type chimera states. Dashed and solid lines indicate unstable and stable curves, respectively. Black: symmetric stationary DSD ($\rho_1 = \rho_3$ and $\Phi_1 = \Phi_3$). Red: asymmetric stationary DSD ($\rho_1 \neq \rho_3$ and $\Phi_1 \neq \Phi_3$). Green: breathing chimeras. Blue: antiphase chimera states.

for $a = 1, 2, 3$. With these definitions, the governing equations of the 9D WS variables are given as [23–25]

$$\begin{aligned} \frac{d\rho_a}{dt} &= \frac{1 - \rho_a^2}{2} \sum_{a'=1}^3 K_{aa'} (\zeta_{a'} \cos(\Phi_{a'} - \Phi_a - \alpha) \\ &\quad - \xi_{a'} \sin(\Phi_{a'} - \Phi_a - \alpha)), \\ \frac{d\Psi_a}{dt} &= \frac{1 - \rho_a^2}{2\rho_a} \sum_{a'=1}^3 K_{aa'} (\zeta_{a'} \sin(\Phi_{a'} - \Phi_a - \alpha) \\ &\quad + \xi_{a'} \cos(\Phi_{a'} - \Phi_a - \alpha)), \\ \frac{d\Phi_a}{dt} &= \frac{1 + \rho_a^2}{2\rho_a} \sum_{a'=1}^3 K_{aa'} (\zeta_{a'} \sin(\Phi_{a'} - \Phi_a - \alpha) \\ &\quad + \xi_{a'} \cos(\Phi_{a'} - \Phi_a - \alpha)) \end{aligned} \quad (6)$$

for $a = 1, 2, 3$.

The OA dynamics can be obtained from the WS dynamics for uniform constants of motion $\psi_j^{(a)} = -\pi + \frac{2\pi(j-1)}{N}$ for $j = 1, \dots, N$, taking the thermodynamic limit $N \rightarrow \infty$. Under this condition, the Kuramoto order parameter is exactly described by $\Gamma_a(t) = \rho_a(t)e^{i\Phi_a(t)}$ since $\gamma_a = 1$ for $a = 1, 2, 3$ and the governing equations read [23, 24, 36]

$$\begin{aligned} \frac{d\rho_a}{dt} &= \frac{1 - \rho_a^2}{2} \sum_{a'=1}^3 K_{aa'} \rho_{a'} \cos(\Phi_{a'} - \Phi_a - \alpha), \\ \frac{d\Phi_a}{dt} &= \frac{1 + \rho_a^2}{2\rho_a} \sum_{a'=1}^3 K_{aa'} \rho_{a'} \sin(\Phi_{a'} - \Phi_a - \alpha) \end{aligned} \quad (7)$$

for $a = 1, 2, 3$.

We will first focus our attention on the chimera states in the thermodynamic limit which live on the Ott-Antonsen manifold. There are two basic types of chimera states, those with two synchronized and one incoherent

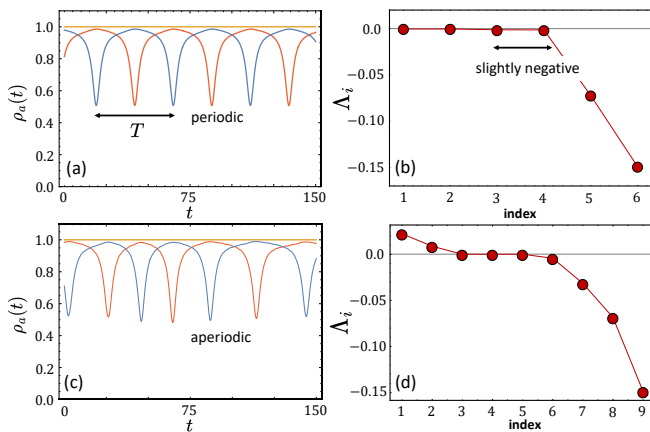


FIG. 2. (a) Radial variables of the 6D OA dynamics (red: first, blue: third population, and orange: second population) and (b) Lyapunov exponents along the antiphase chimera trajectory. (c) Radial variables of the 9D WS dynamics with uniform constants of motion and $N = 20$ and (d) the corresponding Lyapunov exponents. In subfigures: $t > 10^5$ and $A = 0.35$.

population, which was dubbed an SDS-type chimera [36], and one with two incoherent and one synchronized population, so-called a DSD-type chimera. Our analysis shows that the SDS states behave very similar to the chimera states in two-population networks. In particular, the existence of two synchronized populations impede the occurrence of chaotic dynamics. The detailed analysis of the SDS is comprised in Appendix. Here, we concentrate on the DSD chimera states. A bifurcation diagram of DSD-type chimera states is depicted in Fig. 1. We observe two types of DSD chimeras, symmetric ones with $\rho_1 = \rho_3$ and $\Phi_1 = \Phi_3$ that live in a symmetry reduced manifold. Their dynamics within this manifold was studied in Ref. [36]. Our results are in agreement with these data, but reveal that all symmetric DSD states, i.e. also those that were found to be stable within the reduced manifold, have at least one transversally unstable direction and are thus unstable. Not reported before are the asymmetric DSD states with $\rho_1 \neq \rho_3$, $\Phi_1 \neq \Phi_3$ that live off the reduced manifold. Among these states are also stable DSD chimera states (blue line in Fig. 1) in which the two incoherent populations exhibit antiphase character: $\rho_1(t) = \rho_3(t - \frac{T}{2})$ where T is the period of the oscillation. Time series of the three moduli of the order parameter are depicted in Fig. 2 (a). These antiphase DSD chimeras are born in a double-homoclinic cycle of the symmetric stationary DSD, which is point-symmetric in the projection on the $\rho_1\rho_3$ -plane with respect to the diagonal line ($\rho_1 = \rho_3$). The homoclinic bifurcation (Hom) lies very close to a pitchfork bifurcation at which a pair of asymmetric DSD chimeras bifurcates off the symmetric DSD chimera state. The homoclinic bifurcation throws off unstable antiphase DSD chimeras (dashed blue line in Fig. 1) that are at somewhat larger values of A stabilized in a subcritical torus bifurcation (TR). Further increas-

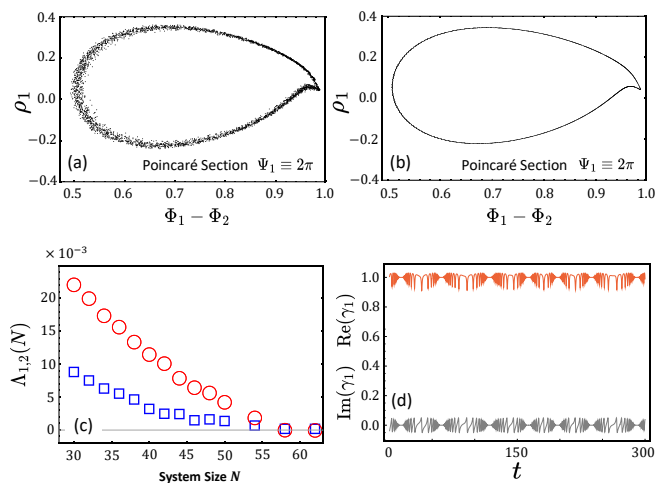


FIG. 3. The Poincaré section for 9D WS dynamics with uniform constants of motion defined by $\Psi_1 \equiv 2\pi$ for (a) $N = 30$ and (b) $N = 100$. (c) Real (orange) and imaginary (gray) parts of γ_1 as a function of time after $t > 10^4$. (d) The largest and the second largest LEs as a function of N for 9D WS dynamics. All the results are obtained with uniform constants of motion of WS dynamics, and the parameter is $A = 0.35$.

ing A , the antiphase chimera state eventually becomes unstable again via a subcritical torus bifurcation.

The dynamics of the antiphase DSD chimera states inherits the symmetry of the solution: $\dot{\Phi}_a(t) = \dot{\Phi}_a(t - T)$, $\dot{\rho}_a(t) = \dot{\rho}_a(t - T)$ for $a = 1, 3$ and $\dot{\Phi}_2(t) = \dot{\Phi}_2(t - \frac{T}{2})$, $\dot{\Phi}_1(t) = \dot{\Phi}_3(t - \frac{T}{2})$ which leads to $\rho_1(t) = \rho_3(t - \frac{T}{2})$. Thus, antiphase chimera states possess just 2 effective degrees of freedom, making chaotic antiphase chimera motions impossible in the OA manifold. This fact can be confirmed by measuring Lyapunov exponents (LEs) (Fig. 2) (b)) [38–40]. There are two zero Lyapunov exponents due to continuous symmetries, i.e., time and phase shift invariance, with two slightly negative and two prominently negative Lyapunov exponents. Hence, the antiphase chimeras in the OA manifold are a stable periodic motion.

In Fig. 2 (c), the antiphase chimera state in a finite-size system obtained from the WS dynamics (Eq. (6)) with uniform constants of motion is shown. Although it displays oscillating antiphase motion of the two incoherent populations similar to the one of the OA dynamics, its motion is not periodic but rather aperiodic, and thus the state does not possess the above mentioned spatio-temporal symmetry. In fact, the Lyapunov analysis (Fig. 2 (d)) clearly shows two positive Lyapunov exponents. In other words, the antiphase chimera state of the small-sized system in the Poisson submanifold (defined as a manifold of finite size N as close as possible to OA manifold, i.e., uniform constants of motion) is chaotic. Furthermore, besides the evidence of the two positive LEs, the chaotic motion of the WS dynamics in small- N systems can be detected in a Poincaré section defined

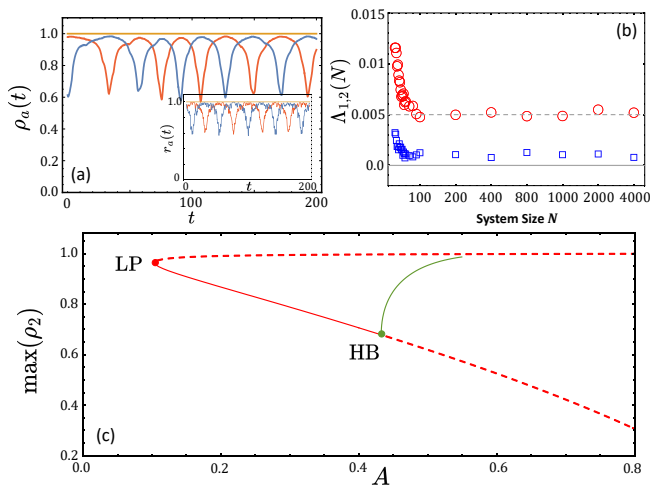


FIG. 4. (a) Radial variables of the WS dynamics with $N = 80$ after $t > 10^5$. Inset: Modulus of Kuramoto order parameters for 9D WS dynamics obtained from Eq. (4). (b) The largest and the second largest LEs as a function of N . The 9D WS dynamics is obtained with nonuniform constants of motion and the microscopic dynamics from a random initial condition. The parameter used here is $A = 0.3$. (c) A bifurcation diagram for SDS-type chimera states. Dashed and solid curves indicate unstable and stable branches, respectively: stationary SDS (red) and breathing SDS chimeras (green).

by $\Psi_1 \equiv 2\pi$ (Fig. 3 (a)) [25]. For $N = 30$, the dynamics in the section follows a scattered motion on a band-like region, as expected for motion on a chaotic attractor.

Opposed to this, the dynamics of the large system with $N = 100$ oscillators resides on a one-dimensional curve in the Poincaré section (Fig. 3 (b)) suggesting that the chaotic motion is restricted to small system sizes. This conjecture is further supported by calculations of the two largest Lyapunov exponents as a function of system size N . In Fig. 3 (c) we can see that the two positive Lyapunov exponents decrease until $N \approx 60$ where they become numerically indistinguishable from zero. The deterministic small-size effect that gives rise to a chaotic motion of antiphase chimeras arises from the influence of $\gamma_a \in \mathbb{C}$ on the WS variables. For small N , γ_a significantly affects the dynamics given by Eq. (6) and renders the WS dynamics different from the OA dynamics. The irregular motion of the real and the imaginary part of γ_a as a function of time of the chaotic chimera state depicted in Fig. 3 (a) is displayed in Fig. 3 (d). As N approaches infinity, $\text{Re}(\gamma_a) \rightarrow 1$ and $\text{Im}(\gamma_a) \rightarrow 0$, so that Eq. (6) becomes identical to Eq. (7) and the aperiodic WS dynamics coincides with the periodic OA motion.

Off the OA manifold, the picture is different. First, we observe that starting from random initial conditions picked from $[-\pi, \pi)$ for simulations of the microscopic dynamics Eq. (1), chaotic antiphase chimera states are observed as well. An example is shown in Fig. 4 (a) where the evolution of the moduli of the Kuramoto order pa-

rameters for the microscopic dynamics (inset) is depicted together with the radial variables of the WS dynamics. The latter is obtained from nonuniform constants of motion that are generated using $\psi_j^{(a)} = (1 - q)\frac{\pi}{2} + \frac{\pi q(j-1)}{N/2}$ and $\psi_{j+N/2}^{(a)} = -(1 + q)\frac{\pi}{2} + \frac{\pi q(j-1)}{N/2}$ with $q = 0.85$ for $j = 1, \dots, \frac{N}{2}$ and for $a = 1, 2, 3$ [23, 24]. The moduli of the Kuramoto order parameters exhibit a qualitatively similar envelope to the radial variables, but with further fluctuations superimposed, as expected from the impact of γ_a in Eq. (4). However, different from the dynamics in the OA manifold, outside of it, the chaotic motion persists for systems as large as $N = 4,000$. The two largest Lyapunov exponents of simulations with nonuniformly distributed constants of motion are shown in Fig. 4 (b). Up to about $N = 100$ they decrease with system size, but then saturate at a positive, non-zero value, indicating that outside the OA manifold the chaotic attractors exist even in the thermodynamic limit. Likewise, the Poincaré section elucidates a similar scattered characteristics to Fig. 3 (e) even for $N = 200$ with nonuniform constants of motion (not shown here). This is different from two-population networks where independent of the system size chaotic dynamics has never been numerically detected.

The simple transition from two to three population networks results thus in a quantum jump in the richness of dynamics. Above we discussed that in the thermodynamic limit, three populations support the coexistence of periodic antiphase chimeras within the OA manifold and chaotic antiphase chimeras outside it. In fact, in addition to these two, the stationary SDS chimera state coexists with these two states in a wide parameter range. The bifurcation diagram shown in Fig. 4 (c) depicts the stability region of the SDS chimera (solid red line). This region overlaps completely with the stability interval of periodic antiphase chimera states, which exist between $0.2 \lesssim A \lesssim 0.4$. Therefore, we evidence the coexistence of three observable chimera states. In addition, the fully synchronized solution is stable in the entire parameter range in which chimera states exist. Yet, within 200 simulations from random initial condition within and off the OA manifold each, at e.g. $A = 0.3$ about half of them lead to antiphase chimeras (periodic in the OA and chaotic off the OA) and the other half of them to SDS chimeras (see Appendix), evidencing that the basins of the three coexisting chimera states occupy most of the phase space.

The dominance of chaotic chimera states in the relatively simple three-population network studied here gives a hint on how rich the order parameter dynamics in more complex network topologies might be.

The authors would like to thank Young Sul Cho for allowing computing facility. This work has been supported by the Deutsche Forschungsgemeinschaft (project KR1189/18-2).

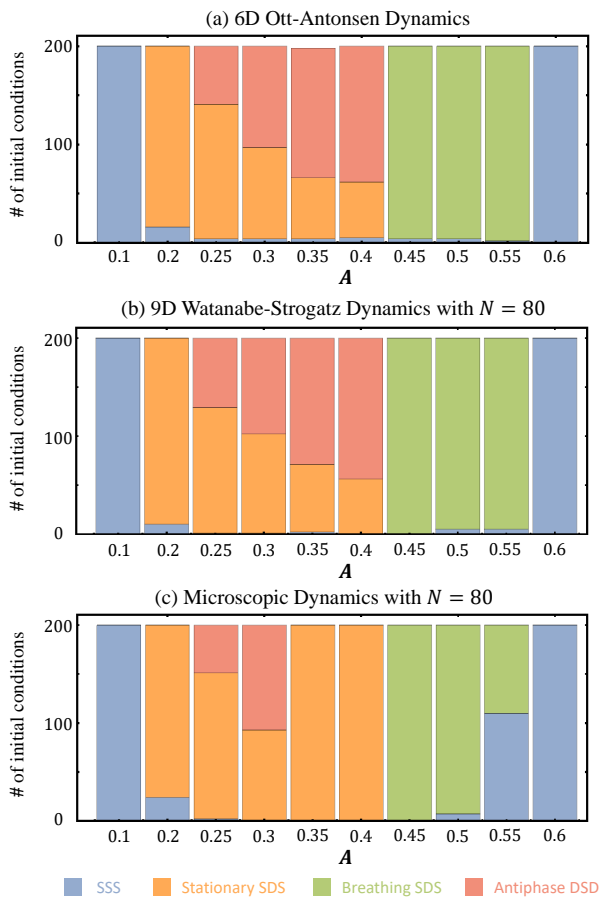


FIG. 5. The number of dynamical states at $t = 20,000$ starting from 200 random initial conditions for different values of A . (a) 6D Ott-Antonsen dynamics. (b) 9D Watanabe-Strogatz macroscopic dynamics with $N = 80$ and uniform constants of motion. (c) $3N$ -dimensional microscopic dynamics with $N = 80$.

Appendix A: Observable Chimera Dynamics

In order to determine the likeliness of observing periodic and chaotic antiphase chimera states, we performed 200 simulations with the OA dynamics (Eq. (7)), the WS dynamics (Eq. (6)) and the microscopic dynamics (Eq. (1)) each. For the WS dynamics, we used uniform constants of motion for $N = 80$. They are all initialized with random initial conditions of the corresponding dynamical variables. The outcome is shown in Fig. 5. In the range between $0.2 \lesssim A \lesssim 0.4$, the coexistence of the stationary SDS chimeras and the antiphase DSD chimeras is observed in the OA and WS dynamics. Here, the antiphase chimeras are periodic. From the microscopic dynamics which corresponds to nonuniform constants of motion in the WS dynamics, chaotic antiphase chimeras are coexisting with stationary SDS chimera states, though in a somewhat smaller parameter interval. Besides these, also breathing SDS chimeras are found, though at different values of A . Note that

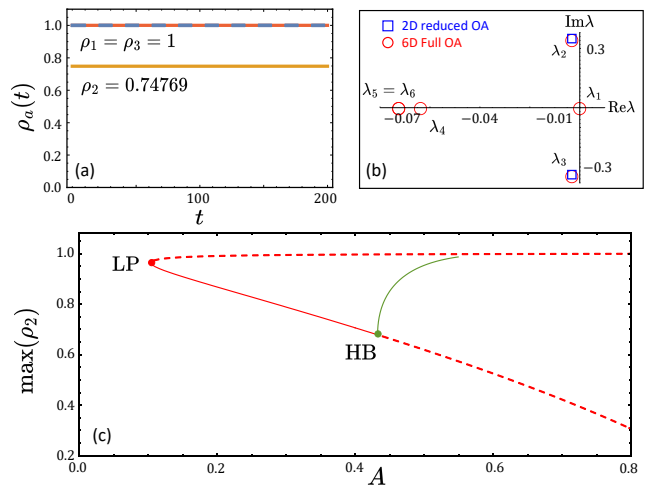


FIG. 6. Stationary SDS chimeras in the 6D OA dynamics. (a) Time evolution of the radial variables of 6D OA dynamics after a transient time of 10^5 units for $A = 0.35$. (b) The eigenvalues of the Jacobian matrix evaluated at the stationary SDS chimera fixed point solution shown in (a) in the complex plane. Red circles indicate the eigenvalues in the 6D OA dynamics, and the blue squares those in the 2D symmetry-reduced manifold. (c) Bifurcation diagram of SDS chimeras. The states are born in a limit point bifurcation (LP). The red dashed and solid curves indicate the location of unstable and stable stationary SDS chimeras, respectively. The green curve shows the maxima of the radial variable of a breathing chimera state emerging in a supercritical Hopf bifurcation (HB).

in Ref. [36], the authors considered only solutions on a symmetry-reduced manifold where the population one and three behave alike in the Ott-Antonsen dynamics. They observed stable stationary/breathing SDS and DSD chimera states in the reduced manifold. However, the stationary and breathing DSD chimera dynamics are unstable in the entire phase space (see Sec. C).

Appendix B: Chimera States of SDS-type

SDS-type chimera states in three-population networks behave similarly to those in two-population networks [18, 25, 26]. In this section, we discuss their dynamical and spectral properties. First, we investigate the stationary SDS chimera states in the 6D Ott-Antonsen manifold. This solution is characterized by $\rho_1(t) = \rho_3(t) = 1$, $\rho_2(t) = \rho_0 < 1$, $\partial_t \Phi_a(t) = \Omega \in \mathbb{R}$ for $a = 1, 2, 3$. Figure 6 (a) shows $\rho_a(t)$ of a stationary SDS at $A = 0.35$. The angular velocity is numerically found to be $\Omega = -2.13448$. In a frame rotating with Ω , this solution can be viewed as a fixed point. Hence we can perform a linear stability analysis and determine the eigenvalues of the Jacobian matrix evaluated at the fixed point solution. In Fig. 6 (b), the six eigenvalues are plotted in the complex plane. All the eigenvalues have non-positive real parts.

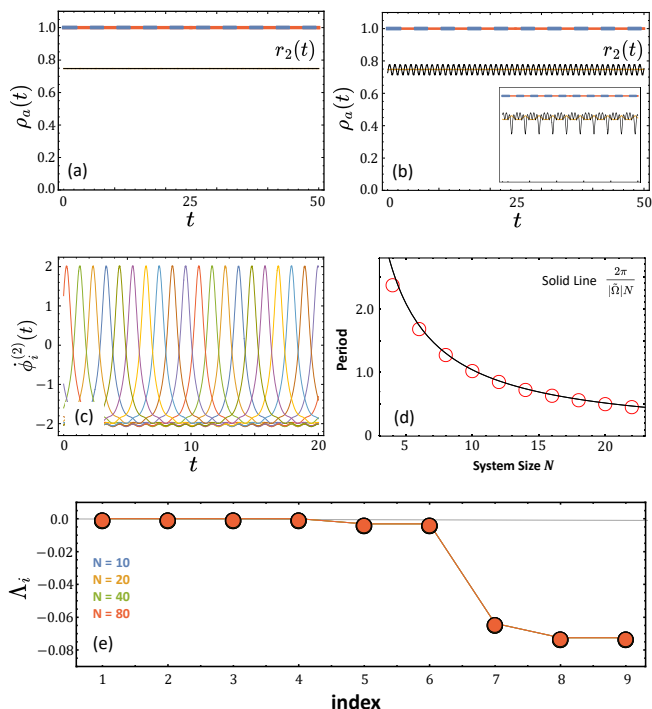


FIG. 7. Stationary SDS chimera states in the 9D Watanabe-Strogatz dynamics. (a,b) Time evolution of the radial macroscopic variables after a transient time of 10^5 units for $A = 0.35$. Blue and red lines indicate $\rho_1(t) = \rho_3(t) = 1$ and the orange line $\rho_2(t) < 1$. The black line shows the modulus of Kuramoto order parameter $r_2(t)$ calculated from the relation between Kuramoto order parameter and the WS variables with uniformly distributed constants of motion: (a) $N = 10$ and (b) $N = 40$. The inset of (b) shows the radial variables and Kuramoto order parameter with nonuniform constants of motion with $N = 10$. (c) Instantaneous phase velocities obtained from Eq. (B5) for $N = 10$ with uniform constants of motion. (d) Period of the modulus of the Kuramoto order parameter as a function of system size N . The red circles are numerically obtained periods and the black solid line is the curve $\frac{2\pi}{|\Omega|N}$. (e) Lyapunov exponents of the 9D macroscopic variables of the WS dynamics.

The eigenvalue, $\lambda_1 = 0$ has an accompanying eigenvector given by $\delta x_1 = (0, 0, 0, \delta a, \delta a, \delta a)^\top$ where $\delta a = 1/\sqrt{3}$, which results from the phase shift invariance and does not affect the stability. Thus, the fixed point solution is stable. The pair of complex conjugate eigenvalues, $\lambda_2 = \bar{\lambda}_3$ corresponds to the eigenvector within the symmetry-reduced manifold: $\delta x_2 = \bar{\delta x}_3 = (0, \delta a, 0, \delta b, \delta c, \delta b)^\top$ for $\delta a, \delta c \in \mathbb{C}$ and $\delta b \in \mathbb{R}$. The real negative eigenvalue λ_4 is related to the perturbation transverse to the symmetry-reduced manifold in the angular direction: $\delta x_4 = (0, 0, 0, \delta a, 0, -\delta a)^\top$ where $\delta a = 1/\sqrt{2}$. The last

two eigenvalues $\lambda_5 = \lambda_6$ are real negative and degenerate.

A bifurcation diagram of the stationary SDS chimera state is depicted in Fig. 6 (c). It follows the same bifurcation scenario as chimeras either in two-population networks [18, 25] or in three-population networks restricted to the 2D reduced manifold [36]. They are created/destroyed in a limit point (LP) bifurcation, creating a stable and an unstable SDS branch. Following the stable branch to large values of A , it is destabilized in a supercritical Hopf bifurcation (HB) generating a stable breathing SDS chimera state. This breathing chimera disappears in a homoclinic bifurcation as the parameter A is further increased (Compare this to Fig. 5 (a) in Ref. [36]).

In Fig. 7, we explore the 9D WS dynamics (Eq. (6) in the main ms) for the stationary SDS chimeras with uniform constants of motion. The global WS dynamics displays a prominent dependence on system size N . For large N , the radial variables (Fig. 7 (a)) are stationary and characterized by $\rho_1(t) = \rho_3(t) = 1$ (red and blue) and $\rho_2(t) = \rho_0 < 1$ (orange coinciding with black, see below). For this solution, we find the angular variable $\partial_t \Phi_a(t) = \Omega$ for $a = 1, 2, 3$, which in fact have the same characteristic as in the 6D OA dynamics above, i.e., $\rho_0 = 0.74769$ and $\Omega = -2.13448$ for $A = 0.35$. The other angular variables read $\partial_t \Psi_a(t) = 0$ for $a = 1, 3$, and $\partial_t \Psi_2(t) = \bar{\Omega} = -0.60369$. For small N (Fig. 7 (b)), the radial variables are slightly fluctuating around the values of the OA dynamics, however, the fluctuations are so small that they can be neglected. The dependence on system size is more evident in the Kuramoto order parameter calculated from Eq. (4) in the main text. For small N , the modulus of the Kuramoto order parameter of the incoherent population shows an oscillating motion along the ρ_0 value (black, in Fig. 7 (b)). Such a secondary oscillation disappears as the system size increases (black, in Fig. 7 (a)), similar to Fig. 4 (a) in Ref. [26]: Both the amplitude and the period are decreasing as N grows. This phenomenon can be understood as follows. Therefore, we use the following form of the Watanabe-Strogatz transformation [21, 22, 24]

$$\tan\left(\frac{\phi_j^{(a)} - \Phi_a}{2}\right) = \frac{1 - \rho_a}{1 + \rho_a} \tan\left(\frac{\psi_j^{(a)} - \Psi_a}{2}\right) \quad (\text{B1})$$

for $a = 1, 2, 3$ and $j = 1, \dots, N$. This transformation directly gives a time derivative of each phase variable in terms of the WS global variables and the constants of motion. Starting with Eq. (B1) as well as its time derivative and omitting for the moment the population index a , we obtain

$$\begin{aligned} \frac{d}{dt}(\phi_j - \Phi) &= 2 \frac{d}{dt} \left[\tan^{-1} \left(g \tan \left(\frac{\psi_j - \Psi}{2} \right) \right) \right] = \frac{2}{1 + g^2 \tan^2 \left(\frac{\psi_j - \Psi}{2} \right)} \left[\dot{g} \tan \left(\frac{\psi_j - \Psi}{2} \right) + \frac{g}{\cos \left(\frac{\psi_j - \Psi}{2} \right)} \left(-\frac{1}{2} \dot{\Psi} \right) \right] \\ &= \frac{g}{\cos^2 \left(\frac{\psi_j - \Psi}{2} \right) + g^2 \sin^2 \left(\frac{\psi_j - \Psi}{2} \right)} \left(\dot{g} \sin(\psi_j - \Psi) - \dot{\Psi} \right) \end{aligned} \quad (\text{B2})$$

for $j = 1, \dots, N$ and $g := \frac{1-\rho}{1+\rho}$. The denominator can be

written, using the trigonometric identity, as

$$\begin{aligned} \cos^2 \left(\frac{\psi_j - \Psi}{2} \right) + g^2 \sin^2 \left(\frac{\psi_j - \Psi}{2} \right) &= \frac{1 + \cos(\psi_j - \Psi)}{2} + g^2 \frac{1 - \cos(\psi_j - \Psi)}{2} \\ &= \frac{1 + \rho^2}{(1 + \rho)^2} + \frac{2\rho}{(1 + \rho)^2} \cos(\psi_j - \Psi) = \frac{1 + \rho^2 + 2\rho \cos(\psi_j - \Psi)}{(1 + \rho)^2} \end{aligned} \quad (\text{B3})$$

The time derivative of g is

$$\frac{\dot{g}}{g} = \frac{-\dot{\rho}(1 + \rho) - \dot{\rho}(1 - \rho) \frac{1 + \rho}{1 - \rho}}{(1 + \rho)^2} = \frac{-2\dot{\rho}}{1 - \rho^2}. \quad (\text{B4})$$

Substituting Eqs. (B3-B4) into Eq. (B2), we obtain the instantaneous phase velocity of each oscillator

$$\dot{\phi}_j^{(a)}(t) = \dot{\Phi}_a - \frac{1 - \rho_a^2}{1 + \rho_a^2 + 2\rho_a \cos(\psi_j^{(a)} - \Psi_a)} \left(\dot{\Psi}_a + \frac{2\dot{\rho}_a}{1 - \rho_a^2} \sin(\psi_j^{(a)} - \Psi_a) \right). \quad (\text{B5})$$

Plugging the macroscopic variables $\rho_2 = \rho_0$, $\dot{\Phi}_2(t) = \Omega$, $\Psi_2(t) = \tilde{\Omega}t + \Psi_2(0)$ and the constants of motion $\psi_j^{(a)}$ uniformly distributed in $[-\pi, \pi]$ into Eq. (B5), we obtain

$$\begin{aligned} \dot{\phi}_j^{(2)}(t) &= \Omega - \frac{\tilde{\Omega}(1 - \rho_0^2)}{1 + \rho_0^2 + 2\rho_0 \cos(\psi_j^{(2)} - \tilde{\Omega}t - \Psi_2(0))} \\ &= \Omega - \frac{\tilde{\Omega}(1 - \rho_0^2)}{1 + \rho_0^2 + 2\rho_0 \cos(\psi_j^{(2)} - \tilde{\Omega}(t - \frac{2\pi}{\tilde{\Omega}}) + \Psi_2(0))} \\ &= \dot{\phi}_j^{(2)}(t - T) \quad \text{where } T := \frac{2\pi}{|\tilde{\Omega}|} \end{aligned}$$

for $j = 1, \dots, N$. This indicates that the instantaneous phase velocity of each oscillator is a periodic function with the period $T = \frac{2\pi}{|\tilde{\Omega}|}$. Furthermore, all the oscillators have the same functional form since they are determined by the same three WS variables (ρ_0, Ω and $\tilde{\Omega}$), and they are equally spaced within the time interval T due to the uniform constants of motion (Fig. 7 (c)). From this fact, we can assume $\dot{\phi}_i^{(2)}(t - \frac{j}{N}T) = \dot{\phi}_{i+j}^{(2)}(t)$ for an arbitrary

$j \in \{1, \dots, N\}$, which gives $\phi_i^{(2)}(t - \frac{1}{N}T) = \phi_{i+1}^{(2)}(t) + C$ for $i = 1, \dots, N$ with $\phi_{N+1}^{(2)} \equiv \phi_1^{(2)}$ where $C \in \mathbb{R}$ is a constant. This assumption [26, 41] leads to

$$\begin{aligned} r_2(t) &= |\Gamma_2(t)| = \left| \frac{1}{N} \sum_{k=1}^N e^{i\phi_{k+1}^{(2)}(t)} \right| \\ &= \left| \frac{e^{-iC}}{N} \sum_{k=1}^N e^{i\phi_k^{(2)}(t - \frac{T}{N})} \right| = \left| \frac{1}{N} \sum_{k=1}^N e^{i\phi_k^{(2)}(t - \frac{T}{N})} \right| \\ &= r_2 \left(t - \frac{T}{N} \right) = r_2 \left(t - \frac{2\pi}{|\tilde{\Omega}|N} \right) \end{aligned} \quad (\text{B6})$$

where the period $\frac{2\pi}{|\tilde{\Omega}|N}$ is decreasing as N increases. In Fig. 7 (d), we numerically measure the periods of the modulus of the Kuramoto order parameter for different sizes N of the incoherent population (red circles) and compare them with $\frac{2\pi}{|\tilde{\Omega}|N}$. The good agreement between the two curves evidences that the stationary SDS chimera state in a small-sized system continuously approaches the

OA dynamics as $N \rightarrow \infty$ in a similar way similar as found for the two-population networks [26]. The stationary SDS chimeras strongly depend on the constants of motion (equivalently, an initial condition of the microscopic dynamics). The inset of Fig. 7 (b), shows the temporal evolution of the radial WS variables and the Kuramoto order parameter for slightly nonuniform constants of motion. Clearly, the time series exhibit non-Poisson chimera features typical for chimeras outside the Poisson submanifold [23, 26].

To determine the stability of these SDS, we determined the Lyapunov exponents (Fig. 7 (e)). Regardless of system size N , the stationary SDS chimeras in 9D WS dynamics are neutrally stable. Two of the zero Lyapunov exponents arise from the two continuous symmetries: the time shift and the phase shift invariance. There are two further zero exponents while the remaining Lyapunov exponents are negative. Thus, SDS chimeras of the 9D WS dynamics are neutrally stable. For the SDS breathing chimeras, they follow the same dynamical and spectral properties as the breathing chimeras in two-population networks [18, 25], i.e. they possess an additional zero Lyapunov exponent [26].

Finally, we explore the $3N$ -dimensional microscopic dynamics. To this end, two different initial conditions are exploited [26, 36]. A PIC (Poisson initial condition) is obtained by determining a fixed point solution of the 2D reduced OA equations, ρ_0 and φ_0 . Then, the initial phases of the incoherent population are obtained by

$$\frac{i - \frac{1}{2}}{N} = \int_{-\pi}^{\phi_i^{(a)}(0)} \frac{1}{2\pi} \frac{1 - \rho_0^2}{1 - 2\rho_0 \cos(\phi - \varphi_0) + \rho_0^2} d\phi$$

for $i = 1, \dots, N$. The initial phases of the synchronized population are selected from a delta distribution. In contrast, an n-PIC (non-Poisson initial condition), i.e. a random initial condition, is generated by randomly selecting phases for all three populations from the uniform distribution of $[-\pi, \pi)$.

In Fig. 8 (a) and (b), the moduli of Kuramoto order parameters calculated from the microscopic dynamics are depicted for a PIC and an n-PIC, respectively, with $N = 10$. For a PIC, the order parameter dynamics shows the same behavior as in Fig. 7 (b), reflecting that a PIC corresponds to uniform constants of motion [25]. As the system size N increases, the amplitude and the period of the secondary oscillation are decreasing and approach the OA dynamics for the same reasoning as discussed above for the WS dynamics. On the other hand, an n-PIC in Fig. 8 (b) gives a non-Poisson chimera motion qualitatively similar to the inset of Fig. 7 (a), corresponding to nonuniform constants of motion.

As far as Lyapunov stability is concerned, both PICs and n-PICs exhibit the same spectral characteristics (Fig. 8 (c)). As far as Lyapunov stability is concerned, both PICs and n-PICs exhibit the same spectral characteristics). Stationary SDS chimeras are neutrally stable with $N - 1$ zero Lyapunov exponents, which explains

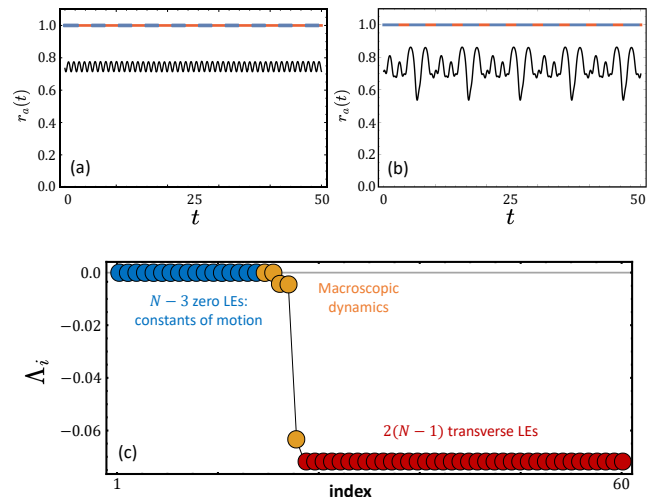


FIG. 8. Stationary SDS chimera states in $3N$ -dimensional microscopic dynamics. (a,b) Time series of the moduli of the Kuramoto order parameters of the three populations with (a) PIC and (b) n-PIC for $N = 10$ and $A = 0.35$ after a transient time of 10^5 units. (c) Lyapunov exponents of the SDS chimeras initiated from a PIC for $N = 20$ and $A = 0.35$.

their strong dependence on the initial condition (or constants of motion). $N - 3$ of the zero Lyapunov exponents (blue) arise from the $N - 3$ constants of motion, the remaining two (orange, zero) are expected to arise from the macroscopic dynamics. The two nearly identical and negative macroscopic Lyapunov exponents (orange) describe the stability with respect to perturbation along the two synchronized populations, the strongly negative one (orange) is related to the WS radial variable of the incoherent population [26]. Moreover, there are $2(N - 1)$ -fold degenerate Lyapunov exponents (red). The covariant Lyapunov vectors (CLVs) [39, 40, 42] corresponding to these Lyapunov exponents, given by

$$\delta x_{\text{trans}} = (\delta a_1, \dots, \delta a_N, 0, \dots, 0, \delta b_1, \dots, \delta b_N)^\top$$

where $\sum_{k=1}^N \delta a_k = \sum_{k=1}^N \delta b_k = 0$, (B7)

reveal that these Lyapunov exponents determine the stability transverse to the synchronized populations.

Appendix C: Chimera States of DSD-type

Figure 5 shows that in none of the simulations a stationary or breathing DSD chimera state was observed. These states will turn out to be unstable later in this section. To investigate their dynamical and spectral properties, we need a very specific initial condition.

In the 6D OA dynamics, we again look for a symmetric fixed point solution of the OA equations obeying $\rho_1(0) = \rho_3(0) = \rho_0 < 1$, $\rho_2(0) = 1$, $\Phi_1(0) = \Phi_3(0) =$

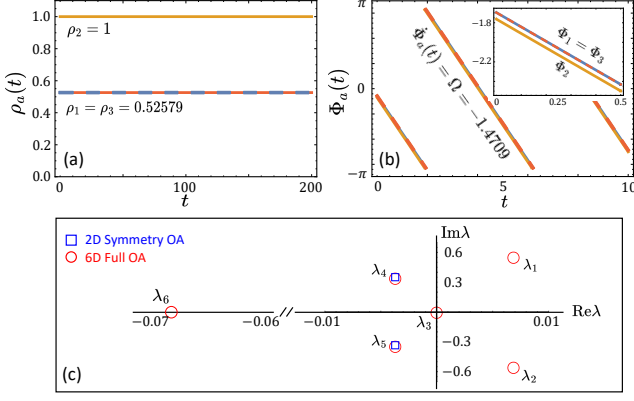


FIG. 9. Unstable stationary DSD chimera state in 6D OA dynamics. (a) Radial variables $\rho_2(t) = 1$ (orange line), $\rho_1(t) = \rho_3(t) = \rho_0 < 1$ (red and blue lines) as a function of time for $A = 0.55$. (b) Time series of the angular variables with the same color scheme as used in (a). In (a) and (b) the first 10^5 time units were discarded. (c) Eigenvalues of the Jacobian matrix evaluated at the DSD solution in the rotating reference frame.

$\varphi_0 \in [-\pi, \pi)$ and $\Phi_2(0) = 0$. In Fig. 9 (a-b), a stationary DSD chimera state from such an initial condition is shown. It is characterized by $\rho_1(t) = \rho_3(t) = \rho_0 < 1$, $\rho_2(t) = 1$, $\Phi_1(t) = \Phi_3(t) = \Omega t + \varphi_0$ and $\Phi_2(t) = \Omega t$. For $A = 0.55$ where a stable stationary DSD chimera can be found in the reduced manifold [36], the numerical values are $\rho_0 = 0.52579$ and $\Omega = -1.4709$. Likewise, in a rotating reference frame with Ω , it is a fixed point solution, which allows us to perform a linear stability analysis and determine the eigenvalues of the Jacobian matrix.

In Fig. 9 (c), the eigenvalues are depicted in the complex plane. Two of them have positive real parts: $\lambda_1 = \bar{\lambda}_2$ with corresponding eigenvectors $\delta x_1 = \bar{\delta x}_2 = (\delta a, 0, -\delta a, \delta b, 0, -\delta b)^\top$ for $\delta a \in \mathbb{C}$ and $\delta b \in \mathbb{R}$. This demonstrates that the unstable directions are transverse to the symmetry-reduced manifold, i.e., the first and the third populations are opposite to each other. The eigenvector corresponding to $\lambda_3 = 0$ is given by $\delta x_3 = (0, 0, 0, \delta a, \delta a, \delta a)^\top$ with $\delta a = 1/\sqrt{3}$, and thus describes a common phase shift. The perturbations corresponding to the pair of complex conjugate eigenvalues $\lambda_4 = \bar{\lambda}_5$ are parallel to the symmetry-reduced manifold: $\delta x_4 = \bar{\delta x}_5 = (\delta a, 0, \delta a, \delta b, \delta c, \delta b)^\top$ for $\delta a, \delta b \in \mathbb{C}$ and $\delta c \in \mathbb{R}$. Finally, $\delta x_6 = (\delta a, \delta b, \delta a, \delta c, \delta c, \delta c)^\top$ for $\delta a, \delta b, \delta c \in \mathbb{R}$ points in the radial direction parallel to the reduced manifold with a common phase shift for all three populations.

On the level of the WS dynamics with uniform constants of motion, we also require a specific initial condition to study the unstable stationary DSD chimera state. Figure 10 (a-c) displays the temporal dynamics of such a DSD chimera when starting (within our numerical resolution) directly on the unstable state. However, imposing a minor perturbation on these initial conditions, the sta-

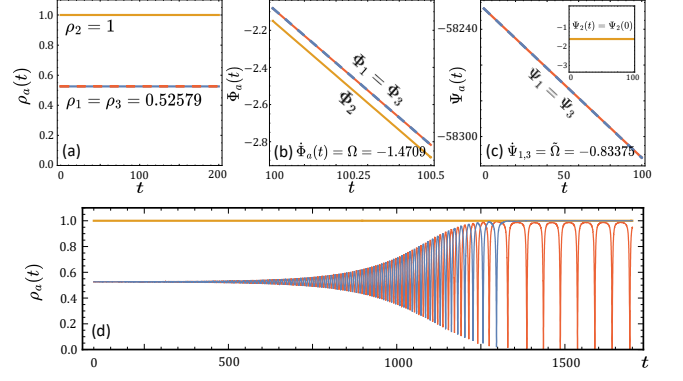


FIG. 10. Unstable stationary DSD chimera states in 9D WS dynamics. (a-c) Time evolution of the 9D Watanabe-Strogatz macroscopic variables after a transient time of 10^5 units with the same color scheme in Fig. 9. (d) Time evolution of the radial variables with a small perturbation on the specific initial condition. $A = 0.55$ and $N = 40$.

tionary DSD chimera state occurs only as a transient, and evolves then through an antiphase oscillation to a breathing SDS chimera state (Fig. 10 (d)).

The Lyapunov exponents of the stationary DSD chimeras in the 9D WS dynamics are shown in Fig. 11 (a). There are two positive Lyapunov exponents: Λ_1 and Λ_2 . This does not indicate a chaotic attractor since any stationary DSD chimera does not involve any chaotic motion and thus should be considered as an unstable solution. Moreover, the CLVs of them have the form $\delta x_{1,2} = (\delta a, 0, -\delta a, \delta b, 0, -\delta b, \delta c, 0, -\delta c)$. This also confirms that the unstable directions of the stationary DSD chimera state are transverse to the symmetry-reduced manifold, i.e., the perturbations of population one and three are opposite to each other. This fact explains why one can obtain DSD chimeras in the reduced manifold but not in the full dynamics.

For the microscopic dynamics, even when starting from a precise PIC (equivalently, uniform constants of motion), we obtain a strange transient. First the system apparently approaches the stationary DSD state in an oscillatory manner and resides close to it for some hundred time units, before it attains a transient antiphase motion and finally reaches a breathing SDS chimera state (Fig. 11 (c-d)).

Since in the microscopic dynamics, we were not able to observe a DSD chimera that lives long enough to investigate the Lyapunov stability, we detour to the 9D WS variables $\rho_a(t)$, $\Psi_a(t)$ and $\Phi_a(t)$ and uniform constants of motion together with the inverse WS transformation from Eq. (B1):

$$\phi_j^{(a)}(t) = \Phi_a(t) + 2 \tan^{-1} \left(\frac{1 - \rho_a(t)}{1 + \rho_a(t)} \tan \left(\frac{\psi_j^{(a)} - \Psi_a(t)}{2} \right) \right)$$

for $j = 1, \dots, N$ and $a = 1, 2, 3$. First, we implement a numerical integration of the 9D WS equations with the very

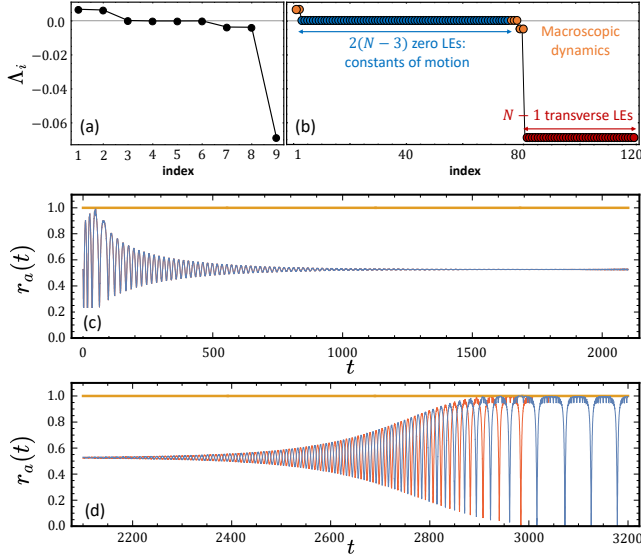


FIG. 11. (a) Lyapunov exponents of the 9D WS dynamics for $N = 40$ corresponding to Fig. 10 (a-c). (b) Lyapunov exponents of the $3N$ -dimensional microscopic dynamics for $N = 40$. (c-d) Time evolution of the moduli of the Kuramoto order parameters for the $3N$ -dimensional microscopic dynamics with $N = 40$ starting from a PIC. $A = 0.55$.

initial condition for the stationary DSD chimeras. Then, we obtain the macroscopic variables as a function of time, which are plugged into the above transformation. This gives the time evolution of each phase variable. Then, the tangent space dynamics is governed by the Jacobian matrix defined by

$$(\mathbf{J})_{ij}(t) = \begin{pmatrix} \frac{\partial \phi_i^{(1)}}{\partial \phi_j^{(1)}} & \frac{\partial \phi_i^{(1)}}{\partial \phi_j^{(2)}} & \frac{\partial \phi_i^{(1)}}{\partial \phi_j^{(3)}} \\ \frac{\partial \phi_i^{(2)}}{\partial \phi_j^{(1)}} & \frac{\partial \phi_i^{(2)}}{\partial \phi_j^{(2)}} & \frac{\partial \phi_i^{(2)}}{\partial \phi_j^{(3)}} \\ \frac{\partial \phi_i^{(3)}}{\partial \phi_j^{(1)}} & \frac{\partial \phi_i^{(3)}}{\partial \phi_j^{(2)}} & \frac{\partial \phi_i^{(3)}}{\partial \phi_j^{(3)}} \end{pmatrix} \quad (\text{C1})$$

evaluated at $\phi_j^{(a)}(t)$ above for $i, j = 1, \dots, 3N$. The tangent linear propagator is defined by $\mathbf{M}(t, t_0) = \mathbf{O}(t)\mathbf{O}(t_0)^{-1}$ where $\dot{\mathbf{O}}(t) = \mathbf{J}(t)\mathbf{O}(t)$ with $\mathbf{O}(0) = I_{3N}$ [39, 40, 42]. Then, we obtain the Lyapunov exponents as

$$\Lambda_i = \lim_{t \rightarrow \infty} \frac{1}{t} \log \frac{\|\mathbf{M}(t, t_0)\delta\mathbf{u}_i(t_0)\|}{\|\delta\mathbf{u}_i(t_0)\|}$$

where $\delta\mathbf{u}_i(t_0)$ belongs to each Oseledets' splitting for $i = 1, \dots, 3N$ [38, 43].

In Fig. 11 (b), we show the Lyapunov exponents of $3N$ -dimensional microscopic dynamics as obtained with the above numerical scheme. There are two positive exponents with CLVs of the form

$$\delta x_{1,2} = (\delta a_1, \dots, \delta a_N, 0, \dots, 0, \delta b_1, \dots, \delta b_N)^\top$$

where $\delta b_i = -\delta a_i$

for $i = 1, \dots, N$, which again elucidates that the unstable directions are transverse to the symmetry-reduced manifold. Also, there are $2(N-3)$ zero Lyapunov exponents (blue) from the constants of motion for the two incoherent populations. The CLVs corresponding to the $(N-1)$ -fold degenerate transverse Lyapunov exponents (red) are given by

$$\delta x_{\text{trans}} = (0, \dots, 0, \delta a_1, \dots, \delta a_N, 0, \dots, 0)^\top$$

where $\sum_{k=1}^N \delta a_k = 0$. (C2)

The other Lyapunov exponents including three zero-valued ones (orange) are expected to occur from the WS macroscopic variables and perturbations along the synchronized population.

-
- [1] L. Larger, B. Penkovsky, and Y. Maistrenko, *Nature Communications* **6**, 7752 (2015).
[2] J. Shena, J. Hizanidis, P. Hövel, and G. P. Tsironis, *Phys. Rev. E* **96**, 032215 (2017).
[3] K. Wiesenfeld and J. W. Swift, *Phys. Rev. E* **51**, 1020 (1995).
[4] S. A. Marvel and S. H. Strogatz, *Chaos* **19**, 013132 (2009).
[5] S. Watanabe and S. H. Strogatz, *Phys. Rev. Lett.* **70**, 2391 (1993).
[6] S. H. Strogatz and I. Stewart, *Sci Am* **269**, 102 (1993).
[7] A. Winfree, *The Geometry of Biological Time*, Interdisciplinary Applied Mathematics (Springer New York, 2013).
[8] R. E. Mirollo and S. H. Strogatz, *SIAM Journal on Applied Mathematics* **50**, 1645 (1990).
[9] C. Bick, M. Goodfellow, C. R. Laing, and E. A. Martens, *The Journal of Mathematical Neuroscience* **10**, 9 (2020).
[10] J. Fell and N. Axmacher, *Nature Reviews Neuroscience* **12**, 105 (2011).
[11] M. Breakspear, *Nature Neuroscience* **20**, 340 (2017).
[12] Y. Kuramoto and D. Battogtokh, *Nonlinear Phenom. Complex Syst.* **5**, 380 (2002).
[13] D. M. Abrams and S. H. Strogatz, *Phys. Rev. Lett.* **93**, 174102 (2004).
[14] M. J. Panaggio and D. M. Abrams, *Nonlinearity* **28**, R67 (2015).
[15] O. E. Omel'chenko, *Nonlinearity* **31**, R121 (2018).
[16] O. E. Omel'chenko, *Nonlinearity* **26**, 2469 (2013).
[17] E. Montbrió, J. Kurths, and B. Blasius, *Phys. Rev. E* **70**, 056125 (2004).
[18] D. M. Abrams, R. Mirollo, S. H. Strogatz, and D. A. Wiley, *Phys. Rev. Lett.* **101**, 084103 (2008).

- [19] E. Ott and T. M. Antonsen, *Chaos* **18**, 037113 (2008).
- [20] E. Ott and T. M. Antonsen, *Chaos* **19**, 023117 (2009).
- [21] S. A. Marvel, R. E. Mirollo, and S. H. Strogatz, *Chaos* **19**, 043104 (2009).
- [22] S. Watanabe and S. H. Strogatz, *Physica D: Nonlinear Phenomena* **74**, 197 (1994).
- [23] A. Pikovsky and M. Rosenblum, *Phys. Rev. Lett.* **101**, 264103 (2008).
- [24] A. Pikovsky and M. Rosenblum, *Physica D: Nonlinear Phenomena* **240**, 872 (2011).
- [25] M. J. Panaggio, D. M. Abrams, P. Ashwin, and C. R. Laing, *Phys. Rev. E* **93**, 012218 (2016).
- [26] S. Lee and K. Krischer, *Chaos* **31**, 113101 (2021).
- [27] M. Wolfrum and O. E. Omel'chenko, *Phys. Rev. E* **84**, 015201 (2011).
- [28] O. E. Omel'chenko, M. Wolfrum, and Y. L. Maistrenko, *Phys. Rev. E* **81**, 065201 (2010).
- [29] O. Burylko, E. A. Martens, and C. Bick, *Chaos* **32**, 093109 (2022).
- [30] E. A. Martens, C. Bick, and M. J. Panaggio, *Chaos* **26**, 094819 (2016).
- [31] S. Guo, M. Yang, W. Han, and J. Yang, *Phys. Rev. E* **103**, 052208 (2021).
- [32] D. Pazó and E. Montbrió, *Phys. Rev. X* **4**, 011009 (2014).
- [33] S. Olmi, *Chaos* **25**, 123125 (2015).
- [34] S. Olmi, E. A. Martens, S. Thutupalli, and A. Torcini, *Phys. Rev. E* **92**, 030901 (2015).
- [35] M. Wolfrum, O. E. Omel'chenko, S. Yanchuk, and Y. L. Maistrenko, *Chaos* **21**, 013112 (2011).
- [36] E. A. Martens, *Phys. Rev. E* **82**, 016216 (2010).
- [37] E. A. Martens, *Chaos* **20**, 043122 (2010).
- [38] A. Pikovsky and A. Politi, *Lyapunov Exponents: A Tool to Explore Complex Dynamics* (Cambridge University Press, Cambridge, 2016).
- [39] F. Ginelli, H. Chaté, R. Livi, and A. Politi, *J. Phys. A: Math. Theor.* **46**, 254005 (2013).
- [40] P. V. Kuptsov and U. Parlitz, *J. Nonlinear Sci.* **22**, 727 (2012).
- [41] S. Lee and K. Krischer, *Phys. Rev. E* **106**, 044210 (2022).
- [42] J. P. Eckmann, *Rev. Mod. Phys.* **57**, 3 (1985).
- [43] V. Oseledets, *Trans. Mosc. Math. Soc.* **19**, 197 (1968).